Optimized Methodology for Reference Region and Image-Derived Input Function Kinetic Modeling in Preclinical PET

Jason Bini, Christine R. Lattin, Takuya Toyonaga, Sjoerd J. Finnema, Richard E. Carson, IEEE Fellow

Abstract—*PET imaging of small animals is often used for assessing biodistribution of a novel radioligand and pharmacology in small animal models of disease. PET acquisition and processing settings may affect reference region or image-derived input function (IDIF) kinetic modeling estimates. We examined four different factors in comparing quantitative results: 1) effect of reconstruction algorithm, 2) number of MAP iterations, 3) strength of the MAP prior, and 4) Attenuation and scatter. The effect of these parameters has not been explored for small-animal reference region and IDIF kinetic modeling approaches. Dynamic PET/CT scans were performed in 3 species with 3 different tracers: house sparrows with [^{11}C]raclopride, rats with [^{18}F]AS2471907 (11βHSD1) and mice with [^{11}C]UCB-J (SV2A). FBP yielded lower kinetic modeling estimates compared to 3D-OSEM-MAP reconstructions, in sparrow and rat studies. Target resolutions (MAP prior strength) of 1.5 and 3.0mm demonstrated reduced V_T in rats but only 3.0mm reduced BP_{ND} in sparrows. Therefore, use of the highest target resolution (0.8mm) is warranted. We demonstrated using kinetic modeling that forgoing CT-based attenuation and scatter correction may be appropriate to improve animal throughput when using short-lived radioisotopes in sparrows and mice. This work provides recommendations and a framework for future optimization of kinetic modeling for preclinical PET methodology with novel radioligands.*

Index Terms—**attenuation, kinetic modeling, positron emission tomography (PET), preclinical, quantification, reconstruction, scatter, small animal.**

I. INTRODUCTION

Kinetic modeling of positron emission tomography (PET) imaging data from small animal experiments is often used for assessing biodistribution of a novel radioligand, pharmacology in animal models of disease, or to aid drug development [1]–[5]. An appropriate kinetic model together with the input function (time course of radioligand in blood or plasma) is used to account for biological factors such as blood flow and local metabolism to determine local tissue concentrations[6]. For reversible radioligands, the regional time concentration can be described by either one- or two-tissue compartment models (1TC, 2TC). For 1TC models, the rate constants K_1 and k_2 describe the kinetics in and out of the tissue from plasma. For the 2TC, there are additional rate constants, k_3 and k_4, defining the rate of receptor binding and disassociation, respectively. The simplest commonly used 2TC kinetic model is for tracers with irreversible uptake (k_4=0) (e.g., [^{18}F]FDG)[7]. The gold-standard 1TC and 2TC models require measurement of the input function, often using blood sampling, e.g., to estimate the distribution volume (V_T), the ratio of the radioligand concentration in the target tissue to that in plasma at equilibrium (K_1/k_2 for 1TC)[8]. When an appropriate reference region is available, i.e., an area devoid of specific binding of the radioligand, the binding potential can be determined [8]. The most common form of the binding potential, BP_{ND}, relates the specific binding in the target organ to the uptake in the reference region; this uptake in the reference region is denoted "non-displaceable", since there is no specific binding which can be blocked or displaced with competing drugs.

Ideally, PET data are acquired in a manner to provide accurate quantification of kinetic parameters; this includes measurement of the radioligand arterial input function and resulting radiolabeled metabolites, with appropriate scanner and reconstruction parameters so that the imaging data are quantitative. Many of the challenges in achieving these goals for kinetic analyses of small-animal PET, such as animal handling, anesthesia, blood sampling, and PET scanner properties, have been discussed previously[9], [10]. For small-animal imaging, the ability to acquire arterial blood and metabolite data is often impossible due to the challenges in blood sampling and/or the volume of blood needed, so that kinetic modeling, e.g., using 1- or 2TC models, cannot be performed [10]. One approach to avoid blood loss is using closed-loop systems; however, these require long set-up times for each animal prior to PET scanning and are not conducive to high animal throughput for short-lived radioisotopes[11].

Thus, to avoid difficulties in arterial blood sampling in small-animal PET, there are many compelling reasons to apply reference region or image-derived input function (IDIF) kinetic modeling approaches[12], [13]. Optimization of kinetic modeling, with respect to IDIFs, has largely been limited to small-animal [^{18}F]FDG PET[14], but remains to be validated for more novel radioligands. For either IDIFs or reference region modeling, the quantitative accuracy of these data is of equal, or even greater importance to that of the primary target region. Given the importance of a quantitatively accurate reference region or IDIF in estimating kinetic parameters, additional aspects of small-animal scanning methodology should be evaluated. Scanner methodology choices that may affect reference region kinetic modeling include the PET reconstruction algorithm, including the number of iterations

and the hyperparameter (*β*) for maximum *a posteriori* (MAP) reconstruction, and correction of attenuation and scatter.

Small-animal PET images are often hindered by the limited resolution of preclinical PET systems[15], [16]. Except for the early time period postinjection, IDIFs and reference regions used for quantification consist of low-activity regions and lack of convergence of 3D ordered subsets expectation maximization (3DOSEM) and MAP algorithms in such regions [17]–[19] will affect parameter estimation. Yao, et al., employed a 3DOSEM algorithm and demonstrated that regions with low radioactivity concentration tend to converge more slowly[20]; however, the effect on reference region kinetic modeling was not explored. Cheng, et al., demonstrated convergence of a MAP reconstruction after 20 iterations in a region with high radioactivity concentration (manufacturer recommended 18 iterations)[21]. However, the number of iterations required for accurate quantification of low radioactivity concentration regions near high radioactivity concentration backgrounds remain to be fully explored for MAP algorithms. In addition to the number of iterations in the MAP reconstruction, the hyperparameter (*β*) is a smoothing parameter used to constrain neighboring voxels and control the resolution of the image[19]. The use of this smoothing parameter and its effects on kinetic modeling estimates with reference region approaches has not been explored for preclinical PET imaging.

Depending on the study protocol, it may be possible to ignore attenuation (AC) and scatter correction (SC) to maximize PET scan throughput by forgoing a CT acquisition (typically ~10min), if used for only attenuation and scatter. Reference region methods may be less sensitive to AC, if lack thereof introduces a scale factor error to the images, which may cancel out for reference kinetic analysis. However, modeling outcome measures estimated from non-attenuation or scatter corrected PET data must be validated. The effects of attenuation and scatter become larger when scanning multiple animals simultaneously. Such paradigms are highly useful with radioligands labeled with carbon-11 [22]. Due to the short half-life of carbon-11 (~20min), and cost of radiosynthesis, it is desirable to scan multiple animals from one radiosynthesis. For example, two mice can be imaged side-by-side in the Inveon PET/CT preclinical system, but this configuration leads to more scatter and attenuation[9], [10]. In addition, the impact of novel animal holders, such as one developed in our lab for house sparrows[23], need to be evaluated with respect to whether their scatter and attenuation effects influence kinetic parameter estimates with reference region approaches[9].

In this study, we examine parameters that affect reference region kinetic modeling in preclinical PET imaging of novel radioligands. Specifically, we evaluated the need for corrections for scatter and attenuation, and selection of PET reconstruction parameters (number of iterations and MAP hyperparameter *β*) using multiple small animal species and radioligands. This work provides a basis for optimizing preclinical PET methodology for reference region kinetic modeling.

II. METHODS

A. House Sparrow [^{11}C]Raclopride Studies

Four house sparrows (*Passer domesticus*)[24] (mean weight: 23.9 ± 1.7 g) were positioned in a recently developed holder for brain imaging of small birds[23]. For reference, house sparrow brain volume is typically ~700 mm³[25], slightly larger than brain volumes of mice (~400-500 mm³)[26]. Animals were injected with 6.6 ± 2.8 MBq of [^{11}C]raclopride, a dopamine receptor type 2 antagonist (mean injected mass: 0.011 ± 0.006 µg). Injections were performed via an intraosseous catheter into the tibiotarsus bone. Listmode PET data were acquired for 60 minutes and rebinned into frames of 8x30s, 3x120s, and 10x300s. All animals had a low-dose CT acquisition after the PET acquisition (Inveon PET/CT, Siemens Preclinical Systems, Knoxville, TN, USA) to provide AC and SC. All PET reconstructions (Section II.D) and ROIs in the striatum (mean 63.8 ± 3.3 mm³) and cerebellum (mean 71.4 ± 2.2 mm³) were extracted from a coregistered canary atlas[27] that was previously validated for use in house sparrows[25]. Coregistration of the atlas to the CT image was performed using rigid registration tools from the Inveon Research Workplace (IRW 4.2, Siemens Medical Solutions, USA). TACs were generated for each ROI and kinetic modeling was performed to estimate BP_{ND} in striatum by applying the simplified reference tissue model (SRTM)[12] and Logan model (*t** of 25min) [28] with the cerebellum reference region.

B. Rat [^{18}F]AS2471907 Studies

Two Sprague-Dawley rats were injected with [^{18}F]AS2471907 via tail vein. [^{18}F]AS2471907 is a radioligand that targets the intracellular enzyme 11β-hydroxysteroid dehydrogenase type 1, which is responsible for converting cortisone to corticosterone (cortisol in humans)[29], [30]. A baseline scan was performed in one rat (weight: 276g) with 17.5 MBq of [^{18}F]AS2471907 (mass: 0.271 µg). A preblocking study was performed in a second rat (309g) with cold AS2471907 (10.8 mg/kg), administered via tail vein injection, 15 minutes prior to radioligand injection of 9.1 MBq of [^{18}F]AS2471907 (mass: 0.192 µg). Listmode PET data were acquired for 60 minutes and rebinned into frames of 8x30s, 3x120s, and 10x300s frames on the preclinical PET/CT scanner. All PET reconstructions were performed as described in Section II.D below. An IDIF was derived from a 2.4mm diameter ROI drawn on 16 consecutive slices (12.8mm axial length) in the abdominal aorta (typical rat abdominal aorta diameter ~2.0mm) during early time frames (0-30s) and was not corrected for partial volume effects. The low levels of radiolabeled metabolites in blood allows for use of an IDIF for this radioligand[30] without inducing considerable bias. Liver and adipose tissue ROIs were drawn on summed images from 20-50 minutes and TACs were generated. 1TC and 2TC models did not fit liver and adipose TACs well. Shorter initial frame durations for image reconstruction (10s) were evaluated with 1TC and 2TC models but still did not provide good fits; liver fitting issues may be due to its dual-blood supply. Therefore, V_T
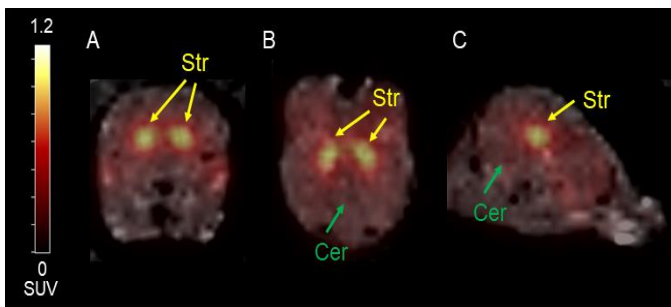
Figure 1 Representative **A)** coronal **B)** axial and **C)** sagittal sparrow [11C]raclopride PET SUV (30-60 min) images overlayed on the co-registered CT, visualizing the striatum (yellow arrows) and cerebellum (green arrows). Reconstruction parameters: 3D-OSEM-MAP (2 OSEM iterations with 16 subsets) followed by 18 MAP iterations, β=0.0023).

Figure 2 Representative sparrow [11C]raclopride TACs for striatum (triangles) and cerebellum (circles) demonstrating the effect of algorithm. FBP shown in orange and MAP (0.8mm) with 18 MAP iterations shown in green.

was estimated using the Logan graphical approach and the aorta TAC as the IDIF and varying t^* from 5 to 25 min and t_{max} (end of fitting period) from 30 to 60min [13].

C. Mouse [11C]UCB-J Studies

Five wild-type mice and eight amyloid precursor protein and presenilin 1 double transgenic mice (mean weight: 30.8 ± 0.8 g) were injected with 6.6 ± 3.0 MBq (mean injected mass: 0.018 ± 0.008 μg) of 11C-UCB-J via retro-orbital injection[31]. 11C-UCB-J is a recently developed radioligand for measuring synaptic density that binds to synaptic vesicle glycoprotein 2A (SV2A)[32]. PET dynamic data were acquired for 120 minutes and binned into frames of 8x30s, 3x60s, 2x120s, and 22x300s frames. Due to technical issues, the CT scan was not available for all scans, so we examined here in a subset of these mice the effect of ignoring attenuation and scatter when performing kinetic modeling. All PET reconstructions were performed, as described below in 'Section II.D.4) Attenuation and scatter'. A mouse brain atlas[33] was coregistered to the PET space, first by manual registration and subsequently with an affine coregistration in FSL[34], [35]. ROIs were extracted for the hippocampus and cerebellum (reference region) and TACs were generated. Kinetic modeling was performed to estimate distribution volume ratio (*DVR)* applying Logan (t* of 25min).

D. PET reconstruction parameters

We examined four different factors in comparing quantitative results. 1) The effect of algorithm: All PET images were reconstructed with the vendor provided software. Images were reconstructed with Fourier Rebinning followed by 2D-FBP (Ramp filter, cutoff at the Nyquist frequency, denoted FBP) or 3D-OSEM-MAP (2 3DOSEM iterations with 16 subsets) followed by 18 MAP iterations, with target resolution 0.8mm (β=0.0023) chosen as the 'gold standard' reconstruction [17]–[19]. 2) The choice of iterations: For the 3D-OSEM-MAP reconstructions, the 3DOSEM component was kept constant while changing the number of MAP iterations (14, 18, 25, 30) (all 3D-OSEM-MAP reconstructions are hence denoted MAP for simplicity). Here, 18 MAP iterations were chosen as the 'gold standard'. 3) The strength of the MAP prior: The vendor
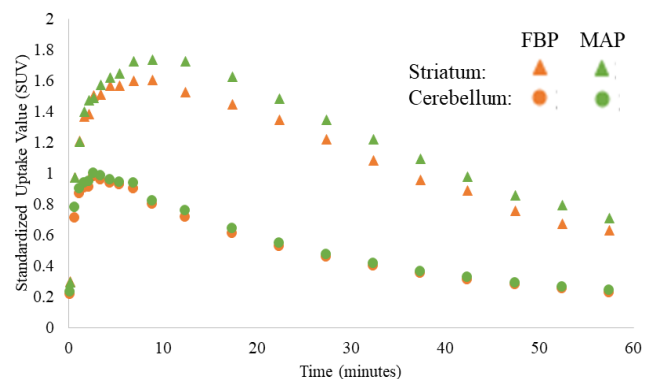
software allows users to select a 'target resolution' based on a hyperparameter (β) with values of 0.0023, 0.0043 and 0.5678, corresponding to manufacturer defined target FWHM values of 0.8, 1.5 and 3.0mm, respectively. Hereafter, all reconstructions are reported using the vendor specified target resolutions and we examined the effect of varying β (target resolution: 0.8, 1.5 and 3.0mm) while keeping a constant 25 MAP iterations, previously shown to provide higher resolution in low radioactivity concentration regions with high radioactivity concentration backgrounds compared to 18 iterations[36]. 4) Attenuation and scatter: Reconstructions were also performed with no AC nor SC (NAC) to determine the effect of removal of corrections on kinetic analyses with selected target resolution of 0.8mm and 25 MAP iterations.

D. Comparison of Methods and Statistics

Comparisons of TAC SUV values are reported in mean ± standard deviation (SD) of percent differences. Quantitative differences in V_T, BP_{ND}, SUV or SUVR-1 are presented as mean ± SD as well as mean ± SD of percent differences. Pearson's correlations between outcome measures from different methods were also calculated when appropriate.

III.   RESULTS

A.   House Sparrow [11C]Raclopride Studies

A representative sparrow [11C]raclopride PET/CT demonstrates visualization of the striatum (target region) and cerebellum (reference region) (Fig. 1).

1. The effect of algorithm

With FBP, [11C]raclopride sparrow reconstructions demonstrated lower values than MAP, with greater differences in striatum (-9.7 ± 2.7%) than cerebellum (-5.3 ± 1.5%) (Fig. 2). The differences varied in the striatum from -1.3% to -9.0% (cerebellum: -4.2% to -7.2%) from 0-5 min vs. -10.6% to -16.1% from 5-60 min (cerebellum: -3.1% to -7.1%). This is likely due to higher radioactivity concentrations in the striatum and poorer recovery coefficients with FBP previously seen in high radioactivity concentration regions [21]. BP_{ND} using
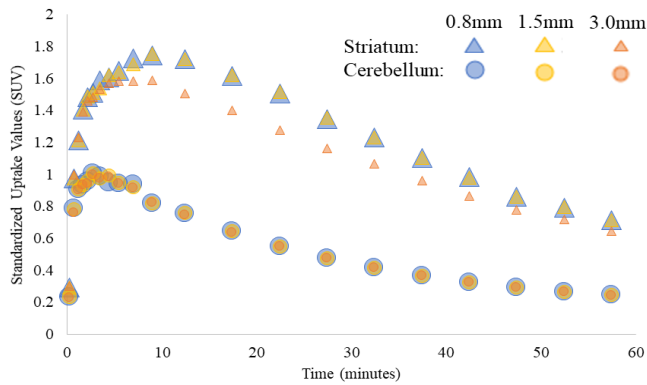
Figure 3 Representative sparrow [^{11}C]Raclopride TACs for striatum and cerebellum for MAP (25 iterations) varying the strength of the prior according to the target resolutions (0.8mm (blue), 1.5mm (yellow) and 3.0mm (orange)). Overlapping symbols are visible due to different sizes.
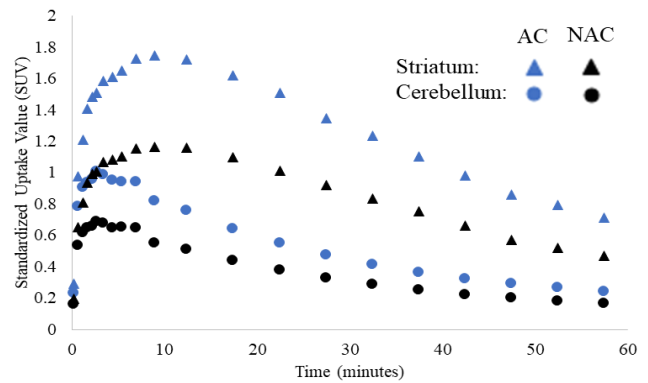

Figure 4 Representative sparrow [^{11}C]Raclopride TACs for striatum and cerebellum for AC and NAC MAP reconstructions (25 iterations, 0.8mm target resolution).

MAP-SRTM was 1.59 ± 0.17, and FBP values were $13 \pm 3\%$ lower (1.38 ± 0.17). BP_{ND} using MAP-Logan was 1.60 ± 0.25. FBP-Logan also had lower BP_{ND} values by $13 \pm 2\%$ (1.38 ± 0.23).

2. MAP iteration number

No differences were found between TACs across all frames as a function of iteration number ranging from 14 to 30 for both cerebellum and striatum. This translated to <1.3% difference in MAP-SRTM or MAP-Logan BP_{ND} estimates as a function of iteration number.

3. The strength of the MAP prior

Changing the prior from 0.8 to 1.5mm target resolution (25 iterations) produced differences of $0.1 \pm 0.4\%$ in cerebellum and striatum MAP-SRTM BP_{ND}. However, with 3mm, lower striatal values were found ($-9.1 \pm 1.9\%$) but not in the cerebellum ($0.4 \pm 0.7\%$) (Fig. 3). MAP-SRTM BP_{ND} (0.8mm) was 1.60 ± 0.18 with <1% change at 1.5 mm (1.59 ± 0.17), but with a $24 \pm 6\%$ underestimation (1.22 ± 0.15) at 3.0mm. Similarly, Logan-MAP BP_{ND} demonstrated a 23% underestimation (1.24 ± 0.19) for 3.0mm but <1.0% overestimation for 1.5mm (1.60 ± 0.24).

4. Attenuation and Scatter Correction

The effect of removing attenuation and scatter correction from MAP in the sparrow studies can be seen in Fig. 4. NAC provided nearly equal underestimation of both cerebellum ($-32.3 \pm 1.1\%$) and striatum ($-33.8 \pm 1.5\%$) TACs. Thus, the mean BP_{ND} underestimations were only $-3.5 \pm 2\%$ (1.55 ± 0.18) and $-3.7 \pm 2\%$ (1.54 ± 0.25) for SRTM and Logan, respectively. Both SRTM and Logan showed very high correlation ($R^2 > 0.98$) between NAC and AC (Fig 5), due to similar NAC underestimation in reference and target regions which cancel out in these methods, since there is little time dependency.

B. Rat [^{18}F]AS2471907 Studies

A representative rat [^{18}F]AS2471907 PET/CT image demonstrates visualization of the liver, adipose tissue and abdominal aorta IDIF (Fig. 6). The effects of reconstruction algorithm and NAC can be seen for TACs of the baseline rat [^{18}F]AS2471907 scan (Fig 7). The Logan graphical approach provided acceptable fits for t^*=5min and t_{max}=30min both liver and adipose tissue in both baseline and blocking scans. Logan graphical approach for t_{max} ranging from 40-60min did not provide acceptable fits regardless of t^*. Logan graphical
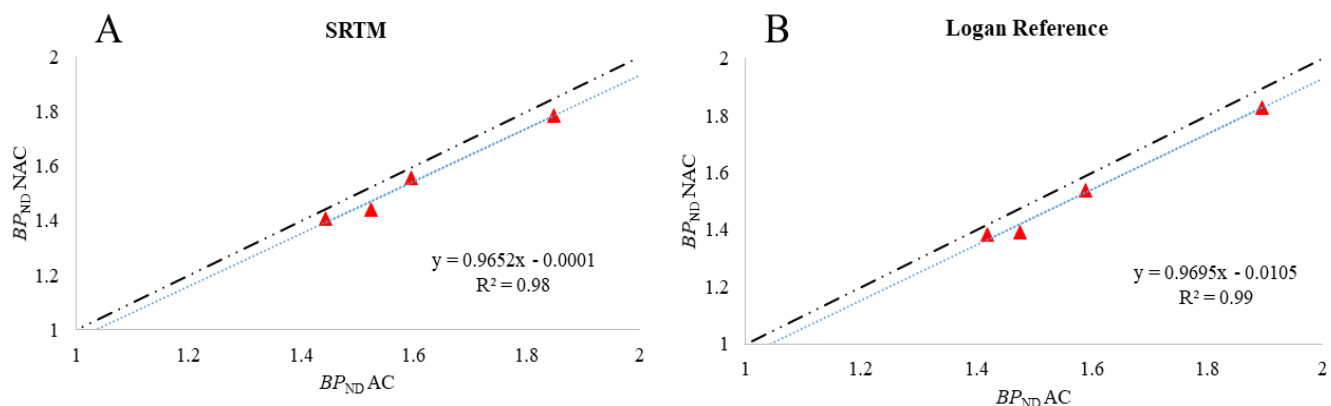

Figure 5. The effect of NAC on sparrow [^{11}C]raclopride striatum BP_{ND} (cerebellum reference) estimates using **A)** simplified reference tissue model **B)** Logan reference model ($t^* = 25$min).
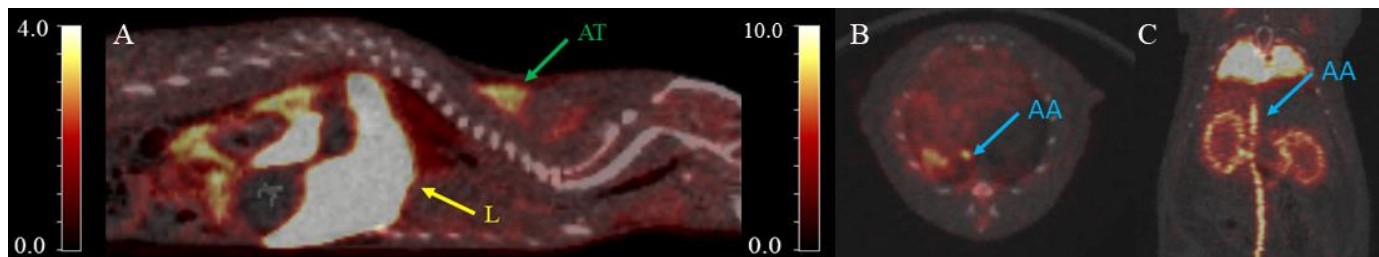
Figure 6 A) Representative rat whole-body sagittal [18F]AS2471907 PET/CT SUV (20-50 min) images visualizing the liver (L, yellow arrow) and adipose tissue (AT, green arrow). Representative **B)** Axial and **C)** Coronal rat [18F]AS2471907 PET/CT SUV (0-1 min) images visualizing the image derived input function from the abdominal aorta (AA, blue arrows). Reconstruction parameters for A-C: 3D-OSEM-MAP (2 OSEM iterations with 16 subsets) followed by 25 MAP iterations, β=0.0023). Blue arrow location in coronal image in **C** corresponds to axial slice shown in **B**.

approach using t^*=5min and t_{max} of 40min or 50min provided lower V_T estimates, which may be influenced by the increasing presence of radiolabeled metabolites or partial volume effects on the input function; therefore, the shortest stable t_{max} of 30min was chosen.

1. The effect of algorithm

In the baseline scan, Logan V_T (MAP 18 iterations) values were 15.1 (liver) and 2.9 (adipose tissue). Similar to the sparrow studies, FBP slightly underestimated blood, liver and adipose tissue TACs (Fig 7). FBP-Logan demonstrated a 5% and 10% underestimation in liver (V_T: 14.4) and adipose tissue (V_T: 2.6), respectively. Underestimation of FBP-Logan V_T values were driven by mean percent differences of FBP TAC SUVs (5-30 min) in the liver and adipose tissue of -6% and -14%, respectively. Blood TAC SUV underestimation was <1% from

5-30 min; however, a 36% underestimation was seen in the first frame.

For the blocking scan, Logan V_T (MAP 18 iterations) was 6.0 (liver) and 2.2 (adipose tissue), respectively. FBP reconstruction demonstrated 7% underestimation in liver (V_T: 5.6) and 24% underestimation in adipose tissue (V_T: 1.6). Mean percent differences of FBP TAC SUVs (5-30 min) of -6% and -10% in liver and adipose tissue drove the underestimation of FBP-Logan V_T in those respective tissues. Similar to baseline, blood TAC differences were <1%.

2. MAP iteration number

For the baseline scan, the effect on V_T estimates of reconstruction and number of iterations showed <1% difference between 14, 25, and 30 iterations in the liver for the baseline scan (liver V_T: 14 iterations 15.1, 25 iterations 15.2, 30
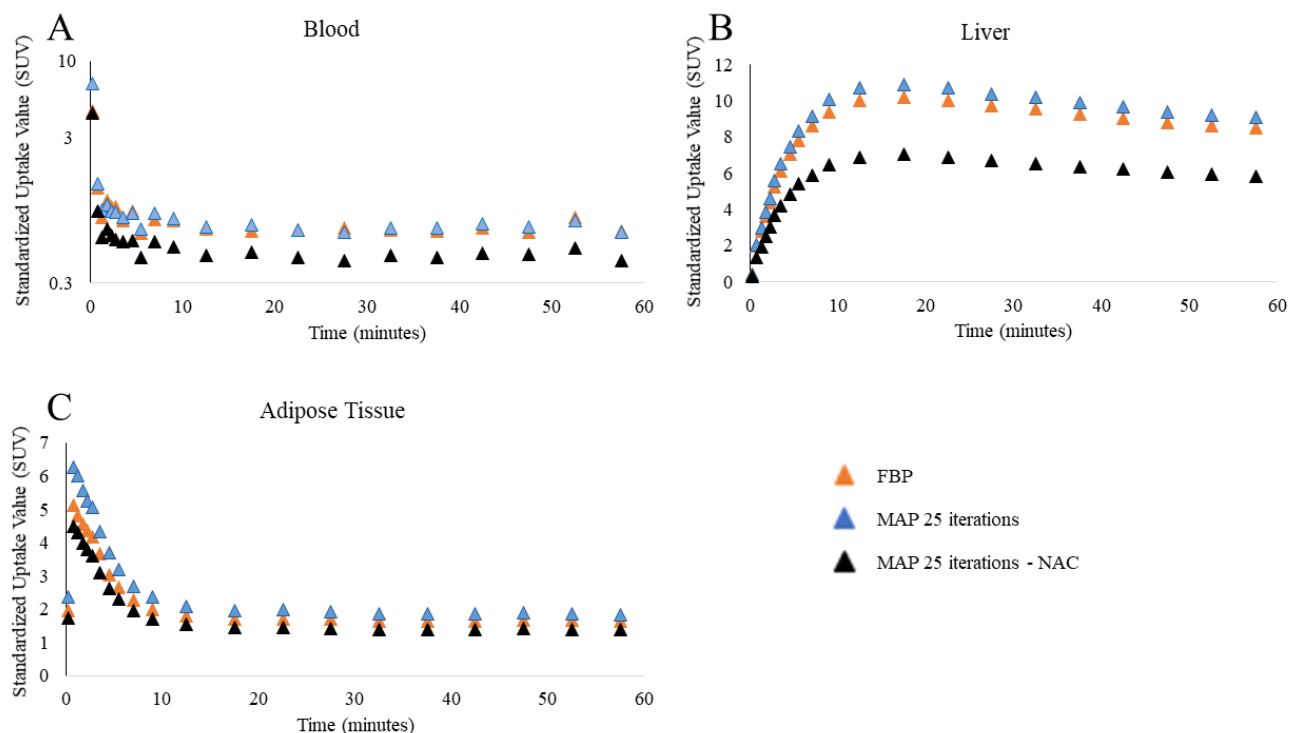

Figure 7 Rat [18F]AS2471907 TACs for the baseline scan using FBP and MAP with AC and NAC (25 iterations; 0.8mm target resolution) reconstruction algorithms. **A)** image derived input function; **B)** liver; **C)** adipose tissue.

iterations: 15.3). No changes in V_T estimates were seen in adipose tissue.

For the blocking scan, there were no differences between 14, 25, and 30 iterations in both liver and adipose tissue. All mean percent differences between TAC SUVs (5-30 min) of blood, liver and adipose tissue for all iteration numbers were ≤1%.

3. The strength of the MAP prior

The effect of changing the MAP prior during the baseline scan from 0.8mm to 1.5mm or 3.0mm demonstrated mean percent differences of <14% underestimation for all regions (blood, liver and adipose tissue). For MAP-Logan (25 iterations; 0.8mm), baseline liver and adipose tissue V_T values were 15.2 and 2.9, respectively. The effect of MAP-Logan on baseline V_T values were minimal in the liver when increasing the target resolution with no change at 1.5mm (V_T: 15.2) and an 8% underestimation at 3.0mm (V_T: 14.0). The effect on baseline V_T values in adipose tissue when increasing the target resolution demonstrated no change at 1.5mm (V_T: 2.9) and a 14% underestimation at 3.0mm (V_T: 2.5). Underestimation of MAP-Logan V_T values in adipose tissue at 3.0mm were driven by a 9% overestimation in mean percent differences of blood TAC SUVs (5-30 min) combined with adipose tissue TAC SUVs that were underestimated by 10%. Less than 1% difference was seen in liver TAC SUVs at 1.5mm or 3.0mm.

For the blocking scan, MAP-Logan (25 iterations; 0.8mm) liver and adipose tissue V_T values were 6.0 and 2.1, respectively. The effect of MAP-Logan on blocking V_T values were less than 7% increases in both liver and adipose tissue for 1.5mm and 3.0mm. In the liver, when increasing the target resolution, there was a 7% overestimation at 1.5mm (V_T: 6.4) and a 5.0% overestimation at 3.0mm (V_T: 6.3). Similarly, the effects on blocking V_T values were small in adipose tissue when increasing the target resolution with no change at 1.5mm (V_T: 2.1) and a 5% overestimation at 3.0mm (V_T: 2.2). All mean percent differences between TAC SUVs (5-30 min) of blood, liver and adipose tissue, when increasing resolution, during blocking scans were ≤4%.

4. Attenuation and Scatter Correction

MAP-NAC V_T estimates demonstrated <1% difference in liver (V_T: 15.1) and a 14% overestimation in adipose tissue (V_T: 3.3). Different underestimation of adipose tissue (-26%) and blood (-35%) of mean percent differences of TAC SUVs (5-30 min) drove overestimation of adipose Logan-NAC V_T estimates. Equal underestimation in liver (-35%), led to minimal difference in liver Logan-NAC V_T estimates. Logan-NAC V_T estimates for the blocking scan demonstrated no difference in the liver (V_T: 6.0) and a 14% overestimation in adipose tissue (V_T: 2.4). Similar to baseline, NAC underestimation of liver (-36%), adipose tissue (-21%) and blood (-37%) was seen in the mean percent difference of TAC SUVs (5-30 min). Larger underestimations in blood than adipose tissue yielded overestimation of adipose tissue V_T, while equal underestimation of liver and blood TACs led to no change in Logan-NAC liver V_T estimates.

C. Mouse [^{11}C]UCB-J Studies

Kinetic analyses for mice scans of [^{11}C]UCB-J (2 mice scanned simultaneously) showed good fits for all mice for Logan
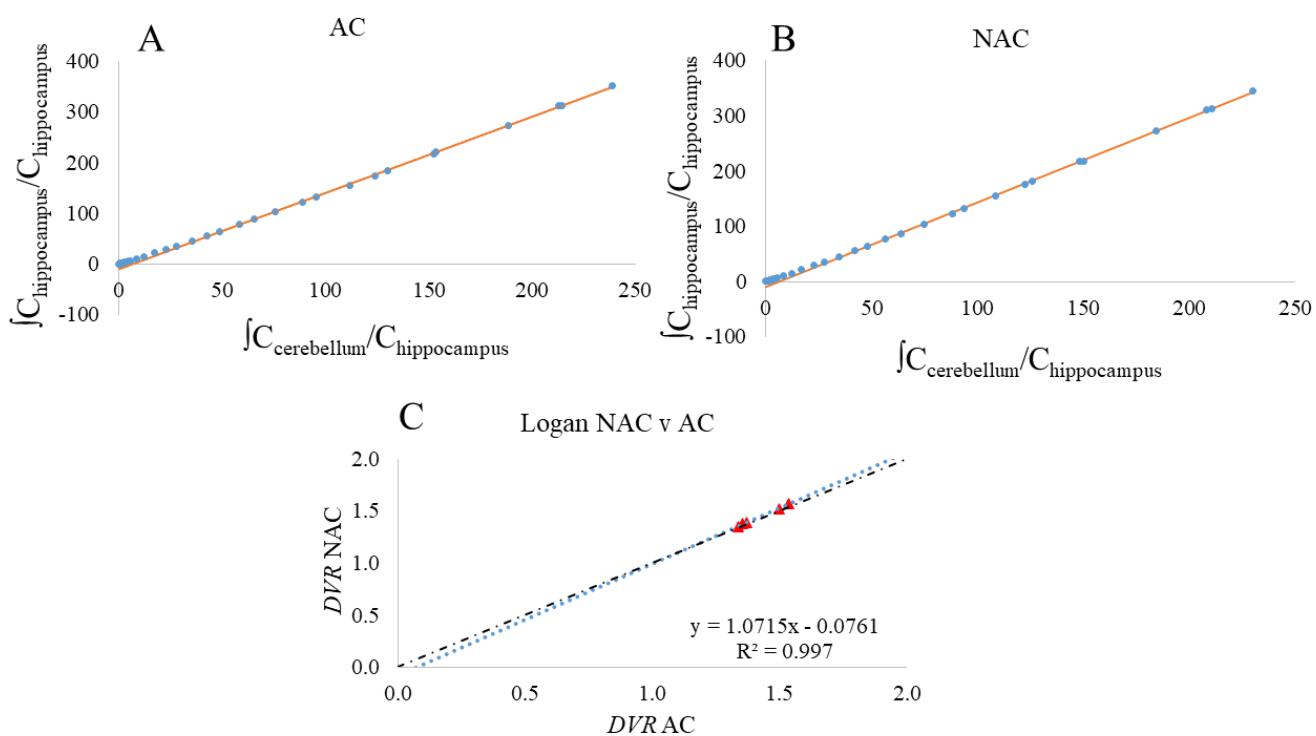

Figure 8 Representative Logan reference graphical analysis for a mouse scan of [^{11}C]UCB-J for **A)** AC and **B)** NAC PET reconstructions. **C)** Pearson's correlation of hippocampus *DVR* for AC and NAC.

graphical analysis using cerebellum as reference region (t*=25min). Figure 8 displays representative fits for AC (Fig. 8A) and no AC/SC (Fig. 8B).

1. Attenuation and Scatter Correction

Mean distribution volume ratio (*DVR)* using AC-Logan was 1.42 ± 0.09. NAC-Logan resulted in minor increases in mean *DVR* for each animal of $1.8 \pm 0.5\%$ (1.44 ± 0.10). The Pearson's correlation comparing AC and NAC (Fig. 8C) was very strong ($R^2 > 0.99$).

IV. DISCUSSION

Reference region methods or those that support use of an IDIF in kinetic modeling have been developed for determination of BP_{ND} and V_T, respectively, such as SRTM[12] and Logan graphical analysis with input function[13]. This work has extended previous studies examining parameters that affect kinetic modeling in preclinical PET imaging[9], [10], [14], [21]. Here we examined: 1) effect of algorithm 2) choice of iterations for MAP reconstructions 3) strength of the MAP prior and 4) forgoing attenuation and scatter correction on data from two radioligands and two species to determine the influence of these parameters on kinetic modeling reference region approaches.

The role of algorithm and iteration number during PET reconstruction was explored previously for the same small animal scanner and the authors concluded, using phantom studies, that the number of iterations required to stabilize MAP reconstruction was 20 iterations, compared to the manufacturer suggested 18[21]. In another study, the role of convergence using 3DOSEM reconstructions suggested that additional iterations were required for low radioactivity concentration regions to converge compared to high radioactivity concentration regions[20]; however, these previous studies did not extend to kinetic analysis. With this in mind, we examined the number of iterations in a MAP PET reconstruction algorithm ranging from 14 to 30 iterations in our sparrow and rat scans. Sparrow and rat TACs showed no major differences with any of the iteration numbers and no differences in kinetic modeling estimates of BP_{ND} or V_T, respectively. The relatively stable BP_{ND} and V_T estimates below 25 MAP iterations was unexpected compared to previous studies that suggested later convergence of low radioactivity concentration (reference) regions using OSEM[21]. The use of system and PSF modeling allows MAP reconstructions to reach convergence with fewer iterations compared to 3DOSEM [18], [19]. This convergence with fewer iterations was seen in our studies for both sparrow and rat reconstructions and could explain the lack of need for further iterations once convergence was reached for low radioactivity concentration regions compared to 3DOSEM without PSF, where differences in iteration numbers were seen between low and high radioactivity concentration regions[20].

The effect of the strength of the MAP prior (changes in target resolution) on quantitative kinetic modeling estimation of BP_{ND} for both SRTM and Logan graphical methods in sparrows demonstrated relatively little effect from 0.8mm to 1.5mm but a relatively large underestimation at 3.0mm. This

underestimation was seen only in the striatum region due to its small size, thus we expect more spill-out from the striatum at lower target resolutions. In a previous study, we demonstrated the 3D isotropic resolution for a ^{22}Na rod source on this scanner to be 1.7mm and 1.9mm for both 0.8mm and 1.5mm target resolutions, respectively[36], which may explain the very minor differences between these two better target resolutions on BP_{ND}.

For rat kinetic modeling, <14% underestimation of V_T was seen in both liver and adipose tissue during baseline scans when changing target resolution from 0.8mm to 1.5mm or 3.0mm. The 14% underestimation in the adipose tissue may appear larger as they represent small absolute differences in V_T in a low activity target region. With the lower target resolution of 3.0mm, the liver was underestimated by 8%, likely due to a larger spill-in to the abdominal aorta (IDIF) which will lead to underestimation of V_T in target regions. In the baseline case, the aorta TAC was increased 9% when using the 3mm target resolution. Despite not correcting for partial volume effects of the IDIF, there was minimal bias when moving from 1.5mm to 3.0mm suggesting that in this case that the net effects of spill-in to the aorta from background regions is low. Naturally, the overall effect of partial volume and the need for correction depends upon the exact imaging situation, and should be explored in future studies.

Scans with displacement of radioligands where high-activity regions at baseline become low-activity regions during blocking may require further consideration. Due to changes in radioligand distribution between baseline and blocking scans in target regions, convergence of both target and reference regions during baseline and blocking scans become important for accurate kinetic modeling estimates.

If molar activity (previously named specific activity[37]) is high enough from a radiosynthesis, sequential rodent scans (perhaps each with multiple animals) may be performed from a single radiosynthesis [9], [10]. For sequential PET scans and injections using the same radiosynthesis, time is important because injection volume and mass dose limitations become significant for small animals. If significant time elapses from radiosynthesis before injection and molar activity is reduced, tracer dose limits for PET imaging may be violated causing physiological perturbations and hindering accurate quantification of radioligand distribution[9], [10]. To increase animal throughput from single radiosyntheses, forgoing attenuation/scatter correction by omitting time-costly CT acquisitions may be possible, if kinetic modeling estimates have been validated for each specific radioligand, animal and kinetic model.

The effect of ignoring scatter correction in kinetic modeling has been examined in several studies. In a human brain phantom study with a scatter fraction of 29% and no scatter correction, Haggstrom, et al, found a positive bias for all four rate constants (K_1, k_2, k_3, and k_4) using a 2-tissue compartment (2TC) model for 3′-deoxy-3′-[^{18}F]fluorothymidine[38]. In a small-animal study examining validation of an animal holder to simultaneously image eight mice with [^{18}F]fallypride, Rominger, et al, found a statistically significant 6% reduction in BP_{ND} when not performing scatter correction estimated using

the Logan graphical analysis method with the cerebellum as a reference region[39]. For studies using rats and rat holders during PET imaging, with larger scatter fractions, ignoring SC tends to increase TACs and subsequent kinetic parameter estimates, while ignoring AC tends to decrease TACs and subsequent kinetic parameter estimates[40], [41]. When using dopaminergic radioligands and reference region approaches, the constant attenuation factor can be ignored or applied in both striatum and cerebellum but ignoring scatter caused different underestimations in each of these regions. However, these differences propogated to ≤10% error in DVR measurements[40]. In a separate study, the equal effects of attenuation correction factors, 16% in both striatum and cerebellum was demonstrated[42]. Additionally, it has been demonstrated that while individual rate constants had relatively large associated errors when estimating [^{11}C]Raclopride uptake in rats, the ratio of constants (e.g., $R_1=K_1/K_1'$) for striatum and cerebellum provided acceptable errors on the fits using reference region kinetic modeling approaches[43]. The sparrow holder was previously reported to cause a fractional PET signal count loss of 13% for the single bird holder and 17% for the dual bird holder[23]. This count loss, with NAC reconstructions, did not propagate to BP_{ND} underestimates in either model due to the nearly equal ~30-35% underestimation in both target and reference regions (striatum and cerebellum, respectively). The production of this holder with 3D-printed, low attenuating materials, provides an excellent example of engineering highly functional devices while also minimizing PET attenuation and scatter[23].

Rat imaging with [^{18}F]AS2471907 demonstrates a reduction in all TACs when ignoring AC and SC (Fig. 7). The very low concentration in the blood during the blocking scans when calculating V_T using blood as an IDIF could account for an overestimation of the target tissue, if by ignoring attenuation and scatter, the blood region is underestimated to a greater degree than the target tissue. In this experiment, we used the rat aorta which is in the center of the rat body where higher attenuation and scattering may occur, especially adjacent to the spine. The total count loss from attenuation and scatter in the rats will be larger than the sparrow or mice since the rats are about 10x the mass of these smaller species. These larger effects in low-activity regions such as the aorta for the rat imaging may lead to larger underestimation of the IDIF during the blocking scan contributing to an increase in V_T. It is important to consider that the use of an IDIF for [^{18}F]AS2471907 was merited due to the relatively low radiolabeled metabolites in the blood [30]. It is also prudent to note that for all IDIF and reference region modeling approaches, radiolabeled metabolites, while not significant in most brain imaging studies (e.g., [^{11}C]Raclopride), must be considered for any novel brain radioligands and whole-body PET imaging ([^{18}F]AS2471907), where radiolabeled metabolites may freely move into target tissue regions. Such considerations may or may not have impacts on the optimal selection of t^* and t_{max}, as demonstrated here by our early t^* and t_{max} choices, but the impact will be different for each radioligand, as we have demonstrated in recent work [44], [45]. A shorter scan time at 30min is able to

balance the radioligand reaching equilibrium while minimizing the potential effects of metabolites circulating in target and/or blood which increase with time. Of note, confirmation of these t^* and t_{max} choices should be confirmed in a larger number of animals. It is worth noting again that 1TC and 2TC kinetic models used in rat studies did not fit the data well, possibly due the dual blood supply input to the liver. Modeling dual blood supply to the liver in preclinical animals has been proposed but remains difficult to date.

Similar to the house sparrow studies, due to the small size of mice (low scatter fractions), when using reference region approaches the effect of ignoring AC/SC have equal effects, in the target and reference regions, that cancel out during kinetic analyses.

Overall, in sparrow and mouse reference region approaches, ignoring AC and SC may be appropriate in certain scan protocols where a CT image acquisition (~10min) can be avoided to increase animal throughput for radioisotopes such as carbon-11 and fluorine-18. One can envision a scenario where three CT scans (~30 min total) as part of a protocol including three sequential 1-hour PET scans, from a single radiosynthesis, could have significant effects on molar activity by the third scan. Such effects can be reduced using reference region approaches that cancel-out equal contributions of scatter and attenuation to the target and reference region approaches. It may also be possible, rather than eliminating the CT scan, to use a shorter lower-quality CT scan for attenuation and scatter correction but it remains to be examined how the low-quality CT would affect attenuation and scatter corrections and kinetic modeling estimates, as well as any direct use of the CT scan (e.g., estimate tumor size).

In these particular cases, brain ROIs were in the center of the object but if a target or reference region was on the edge of the object, while the other was in the center, different spatial effects of attenuation and scatter may not cancel out and may propagate errors to kinetic modeling estimates. For larger animals, such as rats, further caution is warranted when ignoring AC and SC in reconstructions prior to kinetic modeling.

In addition to anatomical considerations, scanner geometry and field-of-view (FOV) size may have different effects on scatter fractions. Distribution in and out of the FOV during the scan time can lead to changes in scatter correction and must be considered for each scanner geometry and FOV length. Given the variability of attenuation and scatter effects, depending on scanner geometry, species and size and location of the target and reference regions and radioligand distribution, it is advisable to examine these effects for each new study.

In this study, we have demonstrated in sparrow and mouse kinetic modeling approaches that ignoring attenuation and scatter correction may be appropriate to improve animal throughput for short-lived radioisotopes. We saw stable but slight underestimation at 18 iterations or less and therefore recommend 25 iterations for modeling applications in line with previous recommendations of >20 iterations for hot regions using a phantom. Target resolutions poorer than 0.8mm demonstrated reduced V_T estimates in rats but did not demonstrate reduced BP_{ND} estimates until 3mm in sparrows. Therefore, use of the highest target resolution (0.8mm) is

warranted. We would like to emphasize that the PET imaging methodology (scatter, attenuation and reconstruction parameters) analyzed here should be validated for each new radioligand and species studied. Keeping this in mind, we have discussed these parameters to sketch a roadmap of steps to consider when validating future preclinical PET kinetic modeling studies.

IV. CONCLUSION

This work provides recommendations for PET imaging methodology for kinetic modeling with reference region or IDIF approaches in several species and radioligands, and in addition, provides a framework for future optimization of kinetic modeling approaches for preclinical PET methodology in novel radioligands.

REFERENCES

[1] S. R. Cherry and S. S. Gambhir, "Use of positron emission tomography in animal research.," *ILAR J.*, vol. 42, no. 3, pp. 219–32, 2001.

[2] R. Yao, R. Lecomte, and E. S. Crawford, "Small-Animal PET: What Is It, and Why Do We Need It?," *J. Nucl. Med. Technol.*, vol. 40, no. 3, pp. 157–165, 2012.

[3] S. Lancelot and L. Zimmer, "Small-animal positron emission tomography as a tool for neuropharmacology," *Trends Pharmacol. Sci.*, vol. 31, no. 9, pp. 411–417, 2010.

[4] W. C. Eckelman, *The Use of Positron Emission Tomography in Drug Discovery and Development*. 2005.

[5] P. M. Matthews, E. Rabiner, J. Passchier, and R. N. Gunn, "Positron emission tomography molecular imaging for drug development.," *Br. J. Clin. Pharmacol.*, vol. 73, no. 2, pp. 175–86, Feb. 2012.

[6] R. E. Carson, "Tracer kinetic modeling in PET: basic science and clinical practice," *Positron Emiss. Tomogr.*, pp. 147–179, 2003.

[7] M. E. Phelps, S. C. Huang, E. J. Hoffman, C. Selin, L. Sokoloff, and D. E. Kuhl, "Tomographic measurement of local cerebral glucose metabolic rate in humans with (F-18)2-fluoro-2-deoxy-D-glucose: Validation of method," *Ann. Neurol.*, vol. 6, no. 5, pp. 371–388, 1979.

[8] R. B. Innis *et al.*, "Consensus nomenclature for in vivo imaging of reversibly binding radioligands," *J Cereb Blood Flow Metab*, vol. 27, no. 9, pp. 1533–1539, 2007.

[9] P. Dupont and J. Warwick, "Kinetic modelling in small animal imaging with PET," *Methods*, vol. 48, no. 2, pp. 98–103, 2009.

[10] C. Kuntner and D. Stout, "Quantitative preclinical PET imaging: opportunities and challenges," *Front. Phys.*, vol. 2, no. February, pp. 1–12, 2014.

[11] M. F. Alf, M. T. Wyss, A. Buck, B. Weber, R. Schibli, and S. D. Krämer, "Quantification of brain glucose metabolism by 18F-FDG PET with real-time arterial and image-derived input function in mice.," *J Nucl Med*, vol. 54, pp. 132–8, 2013.

[12] A.A. Lammertsma and S. P. Hume, "Simplified reference tissue model for PET receptor studies.," *Neuroimage*, vol. 4, no. 4, pp. 153–158, 1996.

[13] J. Logan *et al.*, "Graphical analysis of reversible radioligand binding from time-activity measurements applied to [N-11C-methyl]-(-)-cocaine PET studies in human subjects.," *J. Cereb. Blood Flow Metab.*, vol. 10, no. 5, pp. 740–7, 1990.

[14] M. F. Alf, M. I. Martić-Kehl, R. Schibli, and S. D. Krämer, "FDG kinetic modeling in small rodent brain PET: optimization of data acquisition and analysis.," *EJNMMI Res.*, vol. 3, p. 61, 2013.

[15] Q. Bao, D. Newport, M. Chen, D. B. Stout, and A. F. Chatziioannou, "Performance evaluation of the inveon dedicated PET preclinical tomograph based on the NEMA NU-4 standards.," *J. Nucl. Med.*, vol. 50, pp. 401–408, 2009.

[16] E. P. Visser *et al.*, "Spatial resolution and sensitivity of the Inveon small-animal PET scanner.," *J. Nucl. Med.*, vol. 50, pp. 139–147, 2009.

[17] J. Qi, R. M. Leahy, C. Hsu, T. H. Farquhar, and S. R. Cherry, "Fully 3D Bayesian Image Reconstruction for the EGAT EXACT HR+1," *Ieee Trans. Nucl. Sci.*, vol. 45, no. 3, pp. 1096–1103, 1998.

[18] J. Qi, R. M. Leahy, S. R. Cherry, a Chatziioannou, and T. H. Farquhar, "High-resolution 3D Bayesian image reconstruction using the microPET small-animal scanner.," *Phys. Med. Biol.*, vol. 43, pp. 1001–1013, 1998.

[19] J. Qi and R. M. Leahy, "Resolution and noise properties of MAP reconstruction for fully 3-D PET," *IEEE Trans. Med. Imaging*, vol. 19, no. 5, pp. 493–506, 2000.

[20] R. Yao, J. Seidel, C. A. Johnson, M. E. Daube-Witherspoon, M. V. Green, and R. E. Carson, "Performance characteristics of the 3-D OSEM algorithm in the reconstruction of small animal PET images," *IEEE Trans. Med. Imaging*, vol. 19, no. 8, pp. 798–804, 2000.

[21] J.-C. (Kevin) Cheng, K. Shoghi, and R. Laforest, "Quantitative accuracy of MAP reconstruction for dynamic PET imaging in small animals," *Med. Phys.*, vol. 39, no. May 2011, p. 1029, 2012.

[22] P. Valk, *Positron Emission Tomography: Basic Science and Clinical Practice*, 3rd ed. Springer, 2004.

[23] C. R. Lattin, M. A. Emerson, J. D. Gallezot, T. Mulnix, J. E. Brown, and R. E. Carson, "A 3D-printed modular device for imaging the brain of small birds," *J. Neurosci. Methods*, vol. 293, pp. 183–190, 2018.

[24] C. R. Lattin, D. P. Merullo, L. V. Riters, and R. E. Carson, "In vivo imaging of D2 receptors and corticosteroids predict behavioural responses to captivity stress in a wild bird," *Sci. Rep.*, vol. 9, no. 1, pp. 1–13, 2019.

[25] C. R. Lattin, F. A. Stabile, and R. E. Carson, "Estradiol modulates neural response to conspecific and heterospecific song in female house sparrows: An in vivo positron emission tomography study," *PLoS One*, vol. 12, no. 8, pp. 1–16, 2017.

[26] T. Vincent *et al.*, "Longitudinal Brain size Measurements in App/ps1 Transgenic Mice," *Magn. Reson. Insights*, vol. 4, pp. 19–26, 2010.

[27] M. Vellema, J. Verschueren, V. Van Meir, and A. Van der Linden, "A customizable 3-dimensional digital atlas of the canary brain in multiple modalities," *Neuroimage*, vol. 57, no. 2, pp. 352–361, 2011.

[28] J. Logan, J. S. Fowler, N. D. Volkow, G. J. Wang, Y. S. Ding, and D. L. Alexoff, "Distribution volume ratios without blood sampling from graphical analysis of PET data.," *J. Cereb. Blood Flow Metab.*, vol. 16, no. 5, pp. 834–840, 1996.

[29] J.-D. Gallezot *et al.*, " Imaging the Enzyme 11B-Hydroxysteroid Dehydrogenase Type 1 With Positron Emission Tomography: Evaluation of the Novel Radiotracer 11 C-As2471907 in Human Brain ," *J. Nucl. Med.*, p. jnumed.118.219766, 2019.

[30] S. Bhatt *et al.*, "First in-human PET study and kinetic evaluation of [18 F]AS2471907 for imaging 11β-hydroxysteroid dehydrogenase type 1," *J. Cereb. Blood Flow Metab.*, p. 271678X19838633, 2019.

[31] T. Toyonaga *et al.*, " In vivo synaptic density imaging with 11C-UCB-J detects treatment effects of saracatinib (AZD0530) in a mouse model of Alzheimer's disease. ," *J. Nucl. Med.*, p. jnumed.118.223867, 2019.

[32] S. J. Finnema *et al.*, "Imaging synaptic density in the living human brain," *Sci. Transl. Med.*, vol. 8, no. 348, pp. 348ra96-348ra96, 2016.

[33] M. M. Mirrione, W. K. Schiffer, J. S. Fowler, D. L. Alexoff, S. L. Dewey, and S. E. Tsirka, "A novel approach for imaging brain-behavior relationships in mice reveals unexpected metabolic patterns during seizures in the absence of tissue plasminogen activator," *Neuroimage*, vol. 38, pp. 34–42, 2007.

[34] M. Jenkinson and S. Smith, "Med Image Anal 2001 Jenkinson," vol. 5, pp. 1–14, 2001.

[35] M. Jenkinson, P. Bannister, M. Brady, and S. Smith, "Improved optimization for the robust and accurate linear registration and motion correction of brain images," *Neuroimage*, vol. 17, no. 2, pp. 825–841, 2002.

[36] J. Bini, T. Mulnix, S. Finnema, C. Lattin, G. Cline, and R. Carson, "Maximum a posteriori reconstruction of small-animal dynamic brain PET images on a Siemens Inveon PET/CT," *IEEE Med. imaging Conf.*, 2016.

[37] H. H. Coenen *et al.*, "Consensus nomenclature rules for radiopharmaceutical chemistry — Setting the record straight," *Nucl. Med. Biol.*, vol. 55, pp. v–xi, 2017.

[38] I. Häggström, C. R. Schmidtlein, M. Karlsson, and A. Larsson, "Compartment modeling of dynamic brain PET - The impact of scatter corrections on parameter errors," *Med. Phys.*, vol. 41, no. 11, 2014.

[39] A. Rominger *et al.*, "Validation of the octamouse for simultaneous 18F-fallypride small-animal PET recordings from 8 mice.," *J. Nucl. Med.*, vol. 51, no. 10, pp. 1576–1583, 2010.

[40] D. L. Alexoff *et al.*, "Reproducibility of 11C-Raclopride Binding in the Rat Brain Measured with the MicroPET R4: Effects of Scatter Correction and Tracer Specific Activity," *J. Nucl. Med.*, vol. 44, no. 5, pp. 815–822, 2003.

[41] T. E. Cheng *et al.*, "A rat head holder for simultaneous scanning of two rats in small animal PET scanners: Design, construction, feasibility testing and kinetic validation," *J. Neurosci. Methods*, vol. 176, no. 1, pp. 24–33, 2009.

[42] R. Meyers, S. Hume, and S. Ashworth, "Quantification of dopamine receptors and transporter in rat striatum using a small animal PET scanner," in *Quantification of Brain Function Using PET*, 1996, pp. 12–15.

[43] S. P. Hume *et al.*, "Quantitation of Carbon-11-labeled raclopride in rat striatum using positron emission tomography," *Synapse*, vol. 12, no. 1, pp. 47–54, 1992.

[44] M. Naganawa *et al.*, "Evaluation of Pancreatic VMAT2 Binding with Active and Inactive Enantiomers of [18F]FP-DTBZ in Healthy Subjects and Patients with Type 1 Diabetes," *Mol. Imaging Biol.*, vol. 20, pp. 835–845, 2018.

[45] J. Bini *et al.*, "PET Imaging of Pancreatic Dopamine D3/D2 receptor density with 11 C (+)-PHNO in Type-1 Diabetes Mellitus," *J. Nucl. Med.*, vol. 61, no. 1–7, p. jnumed.119.234013, 2020.